Calibration of colour gradient bias in shear measurement using CANDELS

X. Er[1] ⋆, H. Hoekstra[2], T. Schrabback[3], V. F. Cardone[1], R. Scaramella[1], R. Maoli[4],
M. Vicinanza[1,4,5], B. Gillis[6] L. Miller[7], J. Rhodes[8,9]

[1] *I.N.A.F. - Osservatorio Astronomico di Roma, via Frascati 33, 00040 - Monte Porzio Catone, Roma, Italy*
[2] *Leiden Observatory, Leiden University, PO Box 9513, NL-230 RA, Leiden, the Netherlands*
[3] *Argelander Instutite fuer Astronomie, Auf dem Huegel 71, D-53121 Bonn, Germany*
[4] *Dipartimento di Fisica, Universita di Roma "La Sapienza", Piazzale Aldo Moro, 00185 - Roma, Italy*
[5] *Dipartimento di Fisica, Universita di Roma "Tor Vergata", via della Ricerca Scientifica 1, 00133 - Roma, Italy*
[6] *Royal Observatory, University of Edinburgh, Blackford Hill, Edinburgh EH9 3HJ, UK*
[7] *Department of Physics, Oxford University, keble Road, Oxford OX1 3RH, UK*
[8] *Jet Propulsion Laboratory, California Institute of Technology, 4800 Oak Grove Drive, Pasadena, CA 91109, USA*
[8] *California Institute of Technology, 1200 East California Blvd, Pasadena, CA 91125, USA*

ABSTRACT

Euclid will image about two billion galaxies that can be used to infer cosmological parameters using weak gravitational lensing. Exploiting the precision afforded by these data relies critically on our ability to correct for instrumental effects, such as the convolution by the point spread function (PSF). A complication is the fact that the optical data are obtained using a broad bandpass (550-920 nm) while the diffraction-limited PSF depends on wavelength. This leads to biases in the recovered galaxy shapes because the colours of galaxies vary spatially. We show that the colour-gradient bias can be determined with high accuracy in simulated noisy data. We also find that higher order image distortions, such as flexion, enhance the bias, which may be relevant for the study of lensing in high density regions. We estimate the size of this colour-gradient biases using multi-band observations from the *Hubble* Space Telescope and find correlations with the colours and sizes of the galaxies, but do not observe a significant dependence with redshift. **We need some concluding remark about the impact for Euclid.**

Key words: cosmology, weak lensing, systematics

1 INTRODUCTION

The images of distant galaxies are distorted, or sheared, by the tidal effect of the gravitational potential generated by intervening matter; an effect commonly referred to as weak gravitational lensing (see e.g. Bartelmann & Schneider 2001, for a detailed introduction). The resulting correlations in the shapes can be related directly to the statistical properties of the mass distribution in the Universe, which in turn provide depend on cosmological parameters. Hence weak gravitational lensing by large-scale structure, or cosmic shear, has been identified as a powerful tool for cosmology. The measurement of the signal as a function of cosmological time is sensitive to the expansion history and the growth rate of large-scale structures, and thus can be used to constrain models for dark energy and modified gravity.

A useful measurement of the cosmic shear signal requires averaging over large numbers of galaxies to reduce the uncertainty caused by the intrinsic ellipticities of galaxies. The result is, how-

ever, only meaningful if biases in the shape estimates are negligible. Various instrumental effects change the observed ellipticities by more than the typical lensing signal, which is of order one per cent. The most dominant source of bias is the smearing of the images by the point spread function (PSF), driving the desire for space-based observations (Paulin-Henriksson et al. 2008; Massey et al. 2013). Despite these observational challenges, the most recent cosmic shear studies are starting to yield competitive constraints on cosmological parameters (Heymans et al. 2013; Jarvis et al. 2016; Jee et al. 2016; Hildebrandt et al. 2017). These results are based on surveys of modest areas of the sky, which limits their ability to study the nature of dark energy; to achieve that requires more than an order of magnitude improvement in precision.

Such a measurement is the objective of *Euclid* (Laureijs et al. 2011), the dark energy mission of the European Space Agency (ESA) that will survey the 15 000 deg^2 of extragalactic sky that have both low extinction and zodiacal light. To reduce the detrimental effects of noise on the shape measurements, the images used for the lensing analysis are observed using a wide bandpass (550-920 nm). The much smaller PSF in space-based observations is a

---

⋆ er.xinzhong@oa-roma.inaf.it

major advantage, but the diffraction-limited PSF leads to new complications.

The most prominent one is that the correction for the smearing by the chromatic PSF depends on the spectral energy distribution (SED) of the galaxy of interest (Cypriano et al. 2010; Eriksen & Hoekstra 2017) and ignoring this would lead to significant biases in the case of *Euclid*. Fortunately this can be accounted for using the supporting broad-band observations that are used to derive photometric redshifts for the sources: the correction employs an effective PSF which is derived from the estimate of the observed SED of the galaxy. This correction is sufficient if the SED does not vary spatially. If this is not the case, the underlying brightness distribution, which is needed for an unbiased estimate of the shear, cannot be unambiguously recovered from the observed images. This results in a higher order systematic bias, which we call colour-gradient (hereafter CG) bias. As shown by Semboloni et al. (2013) (S13 in the rest of this paper) the amplitude depends on several factors: the SED of the galaxy, the relative size of the galaxy compared to the PSF, and the width of the bandpass, $\Delta\lambda$. For instance, the bias scales as $\Delta\lambda^2$, and thus is particularly relevant in the case of *Euclid*.

Galaxies show a wide variety in colour gradients, with elliptical galaxies typically showing negative colour gradients (redder in the centre and bluer in the outskirts), with steeper gradients more commonly found in bluer or more luminous early type galaxies (e.g. den Brok et al. 2011; Gonzalez-Perez et al. 2011). Moreover, correlations between colour gradients and the overall colours and luminosities of the galaxies have been inferred (e.g. La Barbera et al. 2010; Kennedy et al. 2016). Hence the relation between galaxy morphology and density may cause the CG bias to vary across the sky and may lead to correlations with the lensing signal itself.

It is important that all systematic sources of biases are accounted for to a level that is smaller than the statistical uncertainties. In the case of *Euclid* this leads to tight requirements, as detailed in Massey et al. (2013) and Cropper et al. (2013). Initial studies by Voigt et al. (2012) and S13 used simulated images to show that the CG bias could be substantial, exceeding nominal requirements for the multiplicative bias in the shear. They also argued that it should be possible to calibrate the bias using *Hubble* Space Telescope (HST) observations of a large sample of galaxies in the F606W and F814W filters. However, their conclusions are based on the analysis of simulated noiseless data. In this work, we revisit the issue of the calibration of CG bias, with a particular focus on determining the bias from data with realistic noise levels.

In Sect. 2, we describe the main concepts and introduce the notation. We present the results from the analysis of simulated images in Sect. 3. In particular we explore the impact of having to use noisy data to measure the CG bias in Sect. 3.2. In Sect. 4 we estimate the CG bias using HST observations from the Cosmic Assembly Near-infrared Deep Extragalactic Legacy Survey (CANDELS; Koekemoer et al. 2011).

2   THE ORIGIN OF COLOUR GRADIENT BIAS

Following the notation of S13, we consider an image of a galaxy, and denote the photon brightness distribution of the image at each position $\boldsymbol{\theta}$ and wavelength λ by $I(\boldsymbol{\theta};\lambda)$, which is related to the intensity $S(\boldsymbol{\theta};\lambda)$ by $I^0(\theta;\lambda) = \lambda S(\boldsymbol{\theta};\lambda)T(\lambda)$, where $T(\lambda)$ is the normalised transmission. We take this to be a top-hat with a width $\Delta\lambda$ around a central wavelength λ_{cen}. The resulting image of the galaxy, observed using a telescope with a PSF $P(\boldsymbol{\theta};\lambda)$ is given by:

$$I^{\text{obs}}(\boldsymbol{\theta}) = \int_{\Delta\lambda} I^0(\boldsymbol{\theta};\lambda) * P(\boldsymbol{\theta},\lambda)\, \mathrm{d}\lambda, \qquad (1)$$

where $*$ denotes a convolution.

A measurement of the ellipticity of a galaxy provides an unbiased (but noisy) estimate of the weak gravitational lensing signal, quantified by the complex shear $\gamma = \gamma_1 + \mathrm{i}\gamma_2$. The ellipticity ϵ in turn can be determined from the second order brightness moments Q_{ij}^0 of the PSF-corrected image $I^0(\theta)$:

$$\epsilon_1 + \mathrm{i}\epsilon_2 \approx \frac{Q_{11}^0 - Q_{22}^0 + 2\mathrm{i}Q_{12}^0}{Q_{11}^0 + Q_{22}^0 + 2(Q_{11}^0 Q_{22}^0 - (Q_{12}^0)^2)^{1/2}} \qquad (2)$$

where the second order brightness moments are given by[1]

$$Q_{ij}^0 = \frac{1}{F} \int I^0(\boldsymbol{\theta})\, \theta_i \theta_j\, \mathrm{d}^2\boldsymbol{\theta} \qquad (i,j = 1,2), \qquad (3)$$

where $F = \int \mathrm{d}^2\boldsymbol{\theta} I^0(\boldsymbol{\theta})$ is the total observed photon flux.

In practice, however, the observed moments are measured from the PSF-convolved image given by Eqn. (1). Moreover, the moments are evaluated using a weight function $W(\boldsymbol{\theta})$ to reduce the effect of noise in the images. Hence, the observed quadrupole moments are given by

$$Q_{ij}^{\text{obs}} = \frac{1}{F_{\text{w}}} \int_{\Delta\lambda} \mathrm{d}\lambda \int \mathrm{d}^2\boldsymbol{\theta}\, I^0(\theta;\lambda) * P(\theta,\lambda)\, \theta_i \theta_j\, W(\boldsymbol{\theta}), \quad (4)$$

where F_{w} is the weighted flux. The use of a weight function biases the observed moments, and the aim of moment-based shape measurement algorithms is to correct for this using estimates of the higher order moments (e.g. Kaiser et al. 1995; Melchior et al. 2011). An alternative approach is to fit sheared, PSF-convolved models to the observed images (e.g. Bridle et al. 2002; Miller et al. 2013); in these fitting methods the profile itself acts as a weight.

S13 showed that the inevitable use of a weight function gives rise to the CG bias. Consequently, the bias depends on the choice of the weight function, and vanishes in the case of *unweighted* moments. In the latter case it possible to determine the PSF-corrected moments Q_{ij}^0 from the observed quadrupole moments because

$$Q_{ij}^{\text{obs}} = Q_{ij}^0 + P_{ij}^{\text{eff}} \qquad (5)$$

for unweighted moments, where P_{ij}^{eff} are the quadrupole moments of the effective PSF, defined as

$$P_{\text{eff}}(\boldsymbol{\theta}) = \frac{1}{F} \int \mathrm{d}\lambda\, P(\boldsymbol{\theta},\lambda)\, F(\lambda), \qquad (6)$$

where $F(\lambda)$ is the photon flux as a function of wavelength, which is directly related to the spectral energy distribution (SED) of the galaxy. Hence the correction for the chromatic PSF requires an estimate of the SED. Eriksen & Hoekstra (2017) have shown that the broadband observations that are used to determine photometric redshifts for *Euclid* can also be used to estimate the effective PSF with sufficient accuracy to meet the stringent requirements presented in Cropper et al. (2013).

We limit our study of the CG bias to the multiplicative bias it introduces, and our approach to quantify the impact on the lensing signal is similar to S13. Figure 1 shows the flowchart of the steps that enable us to evaluate the CG bias. In both cases we start with the same wavelength dependent image $I^0(\boldsymbol{\theta};\lambda)$, but the bottom flow resembles what happens in the actual observations: the

---

[1] We implicitly assume that the moments are evaluated around the position where the dipole moments vanish.
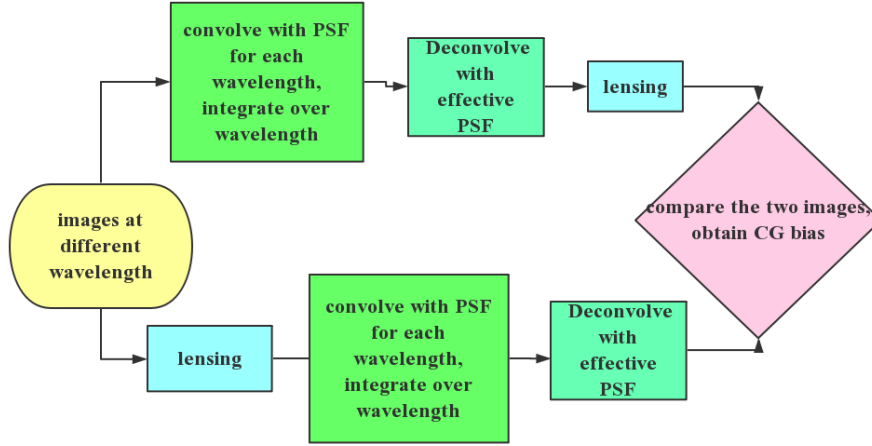
Figure 1. Flowchart describing how the colour-gradient bias is determined. The initial image is the same in both flows, but in the top flow an image without a colour gradient is created to which a shear is applied. In the bottom flow, the image is sheared before the PSF steps are applied. The ellipticities of the resulting images differ slightly, and can be used to quantify the bias that is introduced.

original image is sheared[2] before the convolution with the PSF. The deconvolution with the effective PSF then yields the PSF-corrected shape. In the top flow the PSF steps are applied first, resulting in an image without a colour gradient that is subsequently sheared.

We measure the ellipticities of the resulting images to estimate the CG bias. To reduce noise in our estimate of the multiplicative bias m we use the ring-test method (Nakajima & Bernstein 2007) where we create eight copies of the original galaxy but with different orientations. The ensemble averaged ellipticities then provide an estimate of the multiplicative CG bias, m (we do not explore additive bias here), via

$$m = \frac{\epsilon_i^{\mathrm{CG}}}{\epsilon_i^{\mathrm{NCG}}} - 1, \tag{7}$$

where 'CG' indicates the case where the galaxy has a colour gradient, and 'NCG' is the galaxy with a uniform colour. Note that our approach differs slightly from that in S13, who quantify the response of the observed ellipticity to an applied shear. Hence, they do not apply the last step in the bottom flow (the deconvolution), but rather convolve the final image in the top flow. The steps presented in Fig. 1 yield a more symmetric result, highlighting the fact that the CG bias is the consequence of the fact that the shearing of the image does not commute with the convolution with the PSF. However, we verify in Sect. 3 that we recover the results of S13 (see Fig. 3).

Recently, Huff & Mandelbaum (2017) proposed a technique to infer multiplicative shear calibration parameters that avoids the use of extensive image simulations, such as those described in (Hoekstra et al. 2017). They quantify the sensitivity to a known shear by applying it to the observed data. Hence, their approach follows the top flow in Fig. 1 and thus cannot account for CG bias.

3 COLOUR GRADIENT BIAS IN SIMULATED DATA

The CG bias is a higher order systematic bias, and thus the changes in the measured ellipticities are small. It is therefore important to verify that numerical errors in the calculations are subdominant compared to the small effects we aim to measure. To do so, we compare results from two independent codes that are used to generate the simulated images: one is written in C/C++ and the other uses the python-based GALSIM package (Rowe et al. 2015), which is widely used to created simulated images (e.g. Fenech Conti et al. 2016; Hoekstra et al. 2017).

In the C code we compute the image by multiplying the surface brightness at the centre of each pixel using a sheared Sérsic profile with the pixel area. In the case of GALSIM we use the SHEAR() function (which convolves the image by the pixel). Since we are interested in small differences in the shapes of deconvolved images, we first examined the size of potential numerical errors. We therefore convolved and subsequently deconvolved elliptical images. Comparison of the recovered ellipticities revealed small differences between the codes that ranged from 10^{-7} to 10^{-6}, two orders of magnitude smaller than the CG biases we are concerned with. Hence can safely neglect this numerical artefacts here.

As a further test we compare directly to the results obtained by S13 for two reference galaxy models. The reference galaxies are modeled as the sum of a bulge and disk component. To describe the wavelength dependence of the images we use the galaxy SED templates from Coleman et al. (1980): we use the SED for an elliptical galaxy for the bulge and take the SED of an irregular galaxy for the disk. This choice ensures that the resulting colour gradients are large. The two components are described by a circular Sérsic profile:

$$I_{\mathrm{S}}(\theta) = I_0 \mathrm{e}^{-\kappa \left(\frac{\theta}{a}\right)^{1/n}}, \tag{8}$$

where I_0 is the central intensity, and $\kappa = 1.9992\,n - 0.3271$. For the bulge component we adopt $n = 1.5$ and for the disk we use $n = 1$. The profiles are normalised such that the bulge contains 25% of the flux at a wavelength of 550 nm. The galaxies are circular and the sizes for the bulge and disk for galaxy 'B' are $0''\!.17$ and $1''\!.2$, respectively. The second galaxy 'S' is smaller with sizes of

---

[2] We use $\gamma_1 = 0.05$ and $\gamma_2 = 0.02$ as reference, but we verified that other values yield similar results.
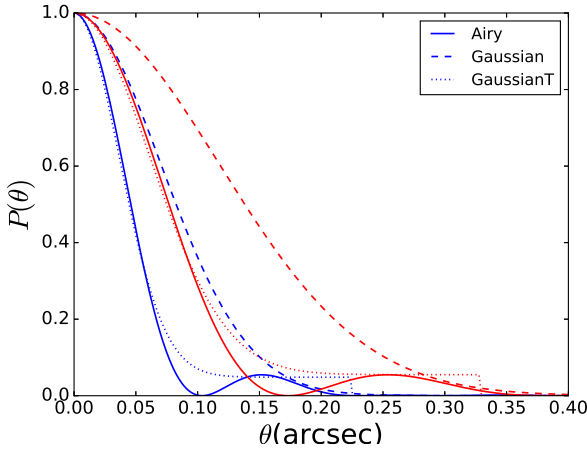
Figure 2. Comparison of the obscured Airy profile (solid), which is a good approximation to the *Euclid* PSF, to PSF1 (Gaussian; dashed) and PSF3 (compact Gaussian and top-hat; dotted) from S13. The profiles for 550 nm are indicated by the blue lines and the results for 920 nm are shown in red.

$0\rlap{.}''09$ and $0\rlap{.}''6$ for the bulge and disk, respectively (also see Table 3 in S13). We create images with a size of 256×256 pixels, and resolution 0.05 arcsec/pixel at wavelengths 1 nm apart and sum these in the range $550 - 920$ nm to mimic the *Euclid* pass-band.

To create the PSF-convolved images we consider several PSF profiles. For a direct comparison with S13 we use their reference PSF1. As discussed in S13 this PSF has a similar size as the nominal *Euclid* PSF, but a steeper wavelength-dependence. Our implementation of the pipeline was able to reproduce the results presented in S13. To better approximate the *Euclid* PSF S13 also considered a model that consists of a compact Gaussian core and an appropriately scaled top-hat (their PSF3). Instead we use here a more realistic obscured Airy profile, which is actually close to the *Euclid* design profile (Laureijs et al. 2011):

$$P(\theta) = \frac{I_0}{(1 - \epsilon^2)^2} \left(\frac{2 J_1(\theta)}{\theta} - \frac{2\epsilon J_1(\epsilon \theta)}{\theta} \right)^2 , \qquad (9)$$

where I_0 is the maximum intensity at the center, ϵ is the aperture obscuration ratio, and $J_1(x)$ is the first kind of Bessel function of order one; x is defined as $x = \pi \theta / \lambda D$. In the case of *Euclid*, $D = 1.2$m and $\epsilon = 1/3$. We compare this model to the Gaussian case and PSF3 from S13 in Fig. 2 at the 550 nm and 920 nm.

As discussed in Sect. 2 the amplitude of the noise bias depends on the width of the weight function that is used to compute the (weighted) quadrupole moments. In Fig. 3 we show the CG bias for the two reference galaxies as a function of $\theta_{\rm w}$, the width of the weight function that is used to compute the quadrupole moments. The results from the C code (dashed lines) and the GALSIM code (dotted lines) agree very well for both the large galaxy 'B' (red lines) and the small galaxy 'S' (blue lines). Given the consistent results between the C and GALSIM code we conclude that numerical errors are negligible in our implementation. In the remainder, we limit the simulations to those generated with `GalSim`.

Figure 3 shows that the CG bias decreases rapidly when the width of the weight function is increased. This allows for an interesting trade-off between CG bias and noise bias. The latter increases with increasing $\theta_{\rm w}$ but relatively slowly (see Fig. 4 in S13). As a proxy for the optimal weight function (which maximizes the signal-to-noise ratio) we adopt the value of the half-light radius in the remainder of this paper. This yields $m = 0.8 \times 10^{-3}$ for galaxy
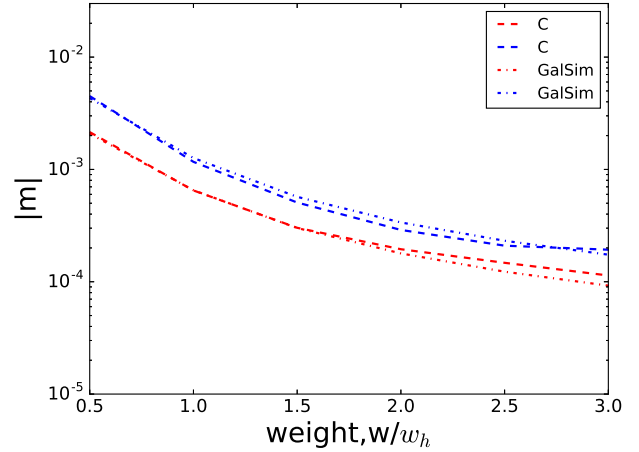
Figure 3. The CG bias in shear versus width of the weight function (in units of the half-light radius $w_{\rm h}$) used to compute the quadrupole moments for the large ('B'; red) and small ('S'; blue) reference galaxy. The galaxies were convolved using the obscured Airy PSF. The dashed (dash-dotted) lines are our results for images simulated using the C (GALSIM) code.

'B' and $m = 2 \times 10^{-3}$ for galaxy 'S', demonstrating that the CG bias is a strong function of galaxy size.

3.1 Impact in high-density regions

The focus of this paper is to quantify the impact of CG bias on cosmic shear measurements, i.e. we consider only small distortions in the shapes of the sources. However, *Euclid* will also enable the calibration of the masses of galaxy clusters with unprecedented precision. Köhlinger et al. (2015) have shown that this should be possible given the accuracy required for the shape measurement algorithms for cosmic shear. This does implicitly assume that the performance does not change in high density environments. Blending does impact the performance (Hoekstra et al. 2017), but can be accounted for. In this section we focus instead on the unexplored question whether the CG bias differs in the central regions of galaxy clusters.

In high density regions, higher order distortions of the images can become dominant. For instance, flexion (the next order after shearing) has been studied as a potential observational tool (e.g. Goldberg & Natarajan 2002; Bacon et al. 2006). Rather than simply shearing the images, as we have done so far, in this section we use the full lens equation to perform ray tracing simulations instead. This enables us to capture the effect of the higher order distortion. For this exercise we use the C code, as it has this functionality fully implemented. As a lens we consider a singular isothermal sphere (SIS) with an Einstein radius $\theta_{\rm E}$; in this case the (tangential) shear is given by $\gamma_{\rm t} = \frac{1}{2}\theta_{\rm E}/\theta$. To minimise numerical effects, the image sizes are increased to 2048×2048 pixels, with a resolution $0\rlap{.}''0125$/pixel.

In Fig. 4 we show the CG bias as a function of the tangential shear for different values of $\theta_{\rm E}$. The red lines indicate the results for the 'B' galaxy and the blue lines show the biases for the 'S' galaxy. For small shears, i.e. far away from the lens, the CG bias converges to the shear-only case that we have studied thus far (the thin horizontal lines). Hence, for cosmic shear studies we can safely ignore this complication. However, as the source approaches the lens, the flexion signal increases, resulting in an increase in the CG bias. The
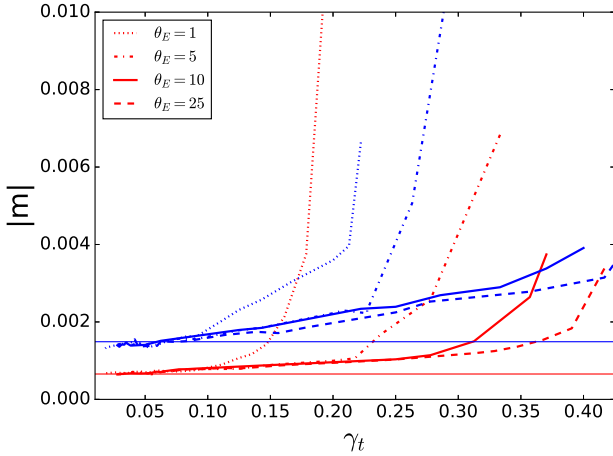
Figure 4. The CG bias versus tangential shear when the full lens equation is used to compute the image distortions. The red lines indicate the resulting CG bias for the 'B' galaxy, whereas the blue lines correspond to the 'S' galaxy. The bias depends on the Einstein radius, $\theta_{\rm E}$, of the lens, and is more prominent for small values of $\theta_{\rm E}$ at a given shear amplitude.

change depends on the value of $\theta_{\rm E}$, because flexion is lower for a given shear when the source is further away from the lens. Hence, the additional CG bias due to higher order distortions is expected to be relatively small for clusters of galaxies (for which $\theta_{\rm E} > 10''$), but it can be relevant for studies of massive galaxies; in this case the Einstein radius is smaller, and the flexion signal larger. Figure 4 shows that for a lens with $\theta_{\rm E} = 1''$ the CG bias rapidly increase when the shear $\gamma > 0.15$, i.e. for $\theta < 3''$. Thanks to the small PSF of *Euclid* it is possible to measure the galaxy-galaxy lensing signal on such small scales, which could in principle provide interesting constraints on the enclosed stellar mass. However, our findings indicate that colour gradients may prevent a robust measurement of the small-scale galaxy-galaxy lensing signal. This warrants further study that is beyond the scope of this paper.

3.2 Calibration of CG bias using simulated HST images

The *Euclid* observations lack high-resolution multi-band images to measure the CG bias directly for each source galaxy. However, the cosmological lensing signal is typically inferred from the ellipticity correlation function, which involves averaging the shapes of large ensembles of galaxies. Provided the average bias that is caused by colour gradients is known for a selection of sources, it is possible in principle to obtain unbiased estimates of the ellipticity correlation function. Here it is particularly important that the correction for the average CG bias accounts for the variation in redshift and colour. The former is relevant for tomographic cosmic shear studies, whereas the latter avoids significant spatial variation in the bias because of the correlation between galaxy colour, or morphology, and density.

S13 showed that HST observations in both the F606W and F814W filters can be used to determine the CG bias to meet *Euclid* requirements. However, S13 did not consider the complicating factor that the HST images themselves are noisy. Although the HST data are typically deeper than the nominal *Euclid* data, and the HST PSF is considerably smaller, it is nonetheless necessary to investigate the impact of noise in more detail. We address this particular

question here, before we determine the CG bias from actual HST data in Sect. 4.

The method to calibrate the CG bias using observations in two bands is described in detail in S13, but here we outline the main steps for completeness. To model the wavelength dependence of the image we use two narrow-band[3] images, each of which is given by:

$$I_i(\boldsymbol{\theta}) = \int_{\Delta\lambda_i} T_i(\lambda)\, I(\boldsymbol{\theta}, \lambda)\, {\rm d}\lambda, \qquad (10)$$

where $T_i(\lambda)$ is the transmission of the ith narrow filter. We assume that for each pixel the wavelength dependence of the image can be interpolated linearly:

$$I(\boldsymbol{\theta}, \lambda) \approx a_0(\boldsymbol{\theta}) + a_1(\boldsymbol{\theta})\lambda. \qquad (11)$$

Eqs.10 and 11 yield a linear set of equations on each pixel, which can be used to solved for the coefficients a_i:

$$T_{0i}a_0(\theta) + T_{1i}a_1(\theta) = I_i(\theta), \quad i = 1, 2, \qquad (12)$$

where we defined

$$T_{ji} = \int_{\Delta\lambda_i} {\rm d}\lambda\, T_i(\lambda)\lambda^j. \qquad (13)$$

We thus obtain approximate galaxy images at each wavelength, which we use to estimate the CG bias, following the same procedure as we used in the previous section.

We first consider the recovery of the CG bias for noiseless observations of the two reference galaxies, as this represents the best-case scenario. We simulate the images in the F606W and F814W filters at different redshifts. We adopt the native sampling of the Advanced Camera for Surveys (ACS) on HST of $0.''05$ pixel^{-1}. As shown in S13, we cannot ignore the blurring of the observed images by the HST PSF; to mimic this we assume an obscured Airy function for a mirror with diameter $D = 2.5$ and obscuration 0.33 as a proxy for the HST PSF. We deconvolve our synthetic HST images and create the images at different wavelengths as the starting point for the flow presented in Fig. 1.

Following S13, we show Fig. 5 the CG bias as a function of redshift for galaxy 'B' (left panels) and 'S' (right panels), demonstrating that the CG bias varies significantly with redshift. The results for the actual CG bias are indicated by the solid black lines, whereas the dashed black lines indicate the recovered values from the noiseless synthetic HST observations in the F606W and F814W filters. The bottom panels show the residuals between the recovered and the true bias. The residual bias is within the target tolerance for *Euclid*, indicated by the grey band, for all redshifts.

We now proceed to explore the impact of noise in the HST images. To do so, we add Gaussian noise to the simulated HST images, where the r.m.s. noise level σ is determined by the signal-to-noise ratio of the galaxy, SNR; the total flux within an aperture of radius $1.5 \times r_{\rm h}$, $F_{\rm tot}$; and the number of pixels within this aperture, $N_{\rm tot}$, such that

$$\sigma = \frac{F_{tot}}{{\rm SNR}\sqrt{N_{tot}}}. \qquad (14)$$

For reference, we compared the input SNR for the two reference galaxies to that estimated by SEXTRACTOR (Bertin & Arnouts

---

[3] To distinguish these filters from the broad VIS pass-band we refer to the F606W and F814W as narrow bands, but acknowledge that these are commonly referred to as broad-band filters and that genuine narrow-band filters are significantly narrower.
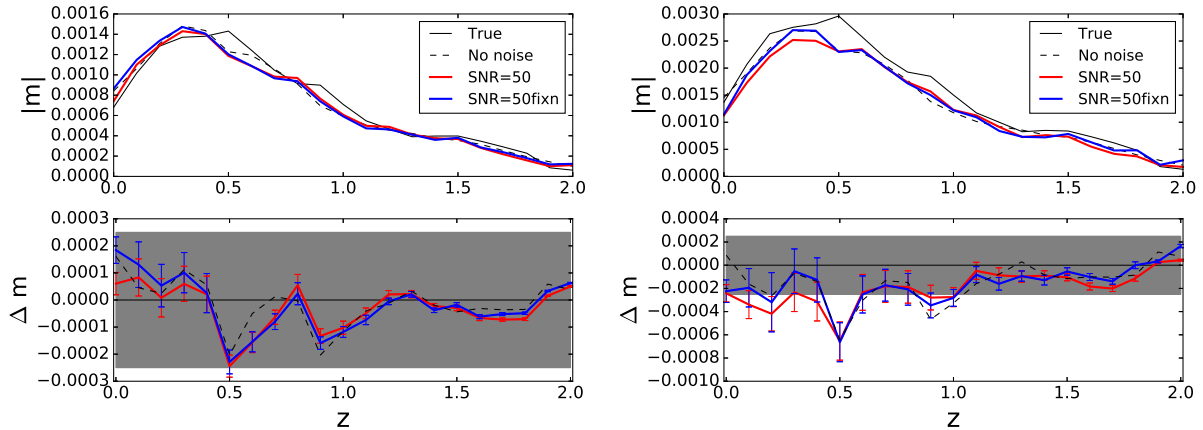
Figure 5. The multiplicative CG bias as a function of redshift for the reference galaxies, with the results for galaxy 'B' shown in the left panel and those for galaxy 'S' in the right panel. The dashed black line is the recovered bias when we mimic noiseless HST observations in two filters. The solid red line indicates the results when we use the best fit GALFIT model in both filters to estimate the CG bias when the simulated HST images have an input SNR= 50 (averaged over 40 noise realisations at each redshift). The blue line shows the results when we fix the Sérsic index in the fit. The bottom panels show the residuals Δm with respect to the true CG bias. The grey band indicates the nominal *Euclid* requirement.

1996). We find good agreement for galaxy 'B' for SNR values ranging from 5 to 50 in both HST filters. The agreement is also good for the 'S' galaxy, but SExtractor returns lower values if the input SNR is larger than 30. We consider two noise levels: a SNR=50 corresponds roughly to a VIS magnitude of $m_{\rm VIS} = 23.7$, a bit brighter than the typical galaxy used in the *Euclid* weak lensing analysis; a SNR=15 approximately corresponds to $m_{\rm VIS} = 25.2$, the faintest galaxies that might be used.

The deconvolution of noisy images is problematic, because the presence of noise will lead to biased estimates of the underlying galaxy. Instead we regulate the problem by assuming that galaxies can be fit by a bulge and disk component, each described by a Sérsic profile. Real galaxies have more complex morphologies, including spiral arms, etc. To first order, however, the radial surface brightness profile is the most important quantity. This can be understood if we consider a galaxy and redistribute the flux in an arbitrary annulus equally into two points on the minor and two points on the major axis. In this case the azimuthally average profile is unchanged, as are the unweighted quadrupole moments. Hence Eqn. (5) is unchanged. The higher order moments are modified, thus affecting realistic shape measurements. However, the ensemble average of such galaxies with random position angles corresponds to the original galaxy. Hence the modified higher order moments are a source of noise, but should not bias the ensemble averaged measurement. This argument is correct in the presence of a axisymmetric PSF, but we note that PSF anisotropy will lead to a coupling with the higher order moments of the galaxy surface brightness and the PSF. Hence, further investigation with realistic morphologies is needed, but our approach should capture most of the CG bias in real data.

We fit the bulge and disk model, convolved with the PSF, to the noisy images in each band and use the best fit model to compute the CG bias. To perform the fit, we use GALFIT (Peng et al. 2010) with the prior constraints on the galaxy parameters (Sérsic index, effective radius, and axis ratio) listed in Table 1. We combine the images in the two filters and use SEXTRACTOR to estimate the center and some of the initial galaxy parameters to be used as the starting point by GALFIT. The resulting best fit images depend somewhat on these initial values, and thus could affect the estimate

parameter	S-606W	S-814W	B-606W	B-814W
n_1	0.5-2.5	0.5-2.5	0.5-2.5	0.5-2.5
n_2	0.5-2.5	0.5-2.5	0.5-2.5	0.5-2.5
$R_{\rm bulge}$	1-10	1-10	3-30	3-30
$R_{\rm disk}$	5-30	5-30	10-60	10-60
q	0.6-1	0.6-1	0.6-1	0.6-1

Table 1. Constraints for the fitting parameters in GALFIT. The first two columns are for two images of the S-galaxy, the other two are the image of B-galaxy. n_1 is the Sersic index for bulge, and n_2 is the Sersic index for disk. The effect radius is given in unit of pixel (0.05 arcsec).

for the CG bias. This will be more important when the SNR of the images is lower. To explore this we perform the fits using two sets of initial parameters: in the first we leave all parameters free, while in the other case we fix the Sérsic index to its simulated value, but leave the other parameters free.

We use the best fit models to compute the CG bias, following the same algorithm as was used to compute the signal in the noiseless case. We show the resulting average inferred CG bias in Fig. 5 for SNR=50 as a function of redshift for the two reference galaxies ('B' in the left panel and 'S' in the right panel). The bottom panels in Fig. 5 show the residuals Δm with respect to the true multiplicative CG bias. To determine the average bias we analyse 6 rotations of the galaxy and use the average value as our estimate of the galaxy ellipticity (Nakajima & Bernstein 2007). Moreover we create 40 noise realisations for each redshift to estimate the statistical uncertainty in our estimate of the multiplicative CG bias, which is given by

$$\sigma_m = |m| \sqrt{\left(\frac{\sigma_{\rm cg} \langle e_{\rm cg}\rangle}{\langle e_{\rm ncg}\rangle^2}\right)^2 + \left(\frac{\sigma_{\rm ncg}}{\langle e_{\rm ncg}\rangle}\right)^2}, \qquad (15)$$

where $\sigma_{\rm ncg}$ and $\sigma_{\rm cg}$ are the uncertainties in the average ellipticities for the images without and with a colour gradient, respectively.

We find that fixing the Sérsic index (blue line) or leaving all parameters free (red line) results in a similar CG bias as a function of redshift. Moreover, the results closely resemble the noiseless case (dashed lines). The residuals presented in the bottom panel of Fig. 5 show that for the SNR=50 case, we expect that the aver-
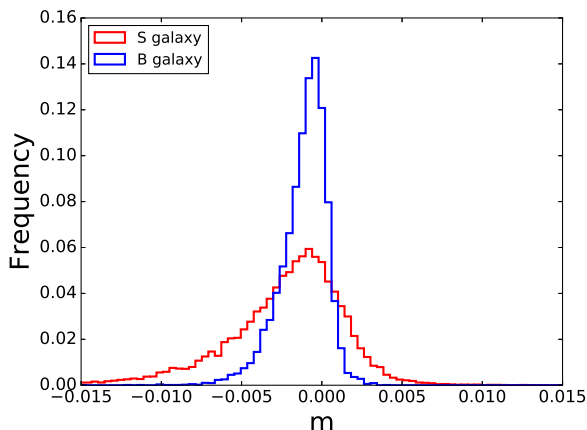
Figure 6. Histogram of the inferred CG bias for the 'B' (blue) and 'S' (red) galaxy when narrow band observations with SNR=15 are used. The histogram combines the results for the different redshifts.

age CG bias can be determined with an overall accuracy that meets the adopted *Euclid* tolerance, indicated by the grey band. Only for the 'S' galaxy is the residual outside the nominal range at low redshifts, but we note that the reference galaxies have rather extreme colour gradients. Moreover, the significant deviations at $z = 0.5$ and 0.9 arise because the adopted SED of the disk (Irr) contains strong emission lines (see Fig. 1 in S13). These lines enter and exit the F606W filter at these redshifts, respectively, and the linear approximation for the wavelength dependence fails. In these, albeit extreme cases, two-band imaging may not be sufficient. To what extent this will affect the estimate of the CG bias requires further study.

The average CG bias for a particular subset of galaxies can be used to correct the ellipticity correlation function. This, however, increases the shape noise, especially if the distribution of biases is broad. Fortunately, Fig. 6 shows the distribution of multiplicative CG bias (combining results for the full redshift range) when the galaxies are detected in the narrow-band images with SNR=15. The distribution is skewed, and as expected, the broadest for the 'S' galaxy. Nonetheless the increase in shape noise due to an empirical correction for CG bias is negligible. We did increase the number of noise realisation to 1000 to ensure robust estimates of the average CG bias as a function of redshift. The resulting CG bias as a function of redshift are shown in Fig. 7. We also show the median bias as a function of redshift, which is slightly different, because the distribution itself is skewed. Nonetheless the bias is recovered to a level that is acceptable for *Euclid*.

3.3 PSF variations narrow-band data

So far we implicitly assumed that the simple axisymmetric PSF used to mimic the HST data is perfectly known. In reality, however, the HST PSF is more complex, and varies spatially and as a function of time. The small field-of-view of ACS typically results in a relatively small number of stars that can be used to model the PSF, although most of the variation can be captured with few parameters (e.g. Schrabback et al. 2010); of these focus variations are the most dominant. We therefore examine next how well the HST PSF properties need to be determined so that they do not affect the CG bias measurement significantly.

To do so, we first generate models where we slightly increase

the PSF size in the two bands by computing the Airy profile when the wavelength in the calculation is increased by a factor 1.05, 1.10 and 1.15 for the three cases. This results in increases in the FWHM of 0.9% between the difference cases. These models are used only in the step where we deconvolve the simulated HST images in the absence of noise. The change in CG bias, Δm as a function of redshift is shown in Fig. 8 for the 'B' galaxy (top panel) and 'S' galaxy (bottom panel). The results for an increase in the PSF size in the F606W band are indicated by the solid, dashed and dotted lines, respectively; the red, green and blue lines indicate the impact of increasing the size of the PSF in the F814W band. The sensitivity to the PSF errors is typically larger for low redshift galaxies, but the change in CG bias is much smaller than the bias itself. As expected, small galaxies are more sensitive to errors in the estimate of the PSF size.

To mimic a more realistic scenario we generated mock star fields using simulated PSFs generated with the TINYTIM tool (Krist et al. 2011). To compute the reference PSFs at the various positions on the detector in the F606W and F814W filters we used the default parameters where possible, including the appropriate camera, detector, and filter passband settings for each image. We adopt the K7V spectrum for the SED, which represents a typical stellar SED in the sample (the choice of a fixed spectrum for stars was found to have a negligible impact on the models.). We select stars with a signal-to-noise ratio larger than 50, and ensure there are no detected objects within 1 arcsecond (20 pixels), and outlier rejection is performed in the fitting procedure. The postage stamps of the star images for each filter are normalised and then stacked using inverse-variance weighting. This PSF is then used to determine the colour gradient bias from the synthetic HST images of the two reference galaxies (which are convolved with an obscured Airy function for a mirror with diameter D = 2.5 and obscuration 0.33 as a proxy for the HST PSF). The blue lines in Fig. 9 show the resulting difference in CG bias for the 'B' (top panel) and 'S' galaxy (bottom panel) as a function of redshift. Although this represents a relatively significant mismatch in PSFs, the change in bias is quite small.

To mimic modeling errors that would occur in reality we select simulated PSF images at a nearby position on the detector (from a grid of points) and fitted for the focus values. The corresponding model PSFs are stacked using the same weights as before. The resulting change in CG bias for the 'B' (top panel) and 'S' galaxy (bottom panel) as a function of redshift as shown by the red lines. The differences between the two TinyTim PSF models is well within requirements, even for the 'S' galaxy. These results therefore confirm the conclusion of S13 that the uncertainty in the HST PSF model has a negligible impact on the determination of the CG bias.

4 MEASUREMENT FROM HST OBSERVATIONS

In the previous section we confirmed the conclusion from S13 that it is possible to determine the CG bias from HST observations in the F606W and F814W filters. Importantly, we demonstrated that the presence of noise in the actual data should not bias the results significantly. We therefore proceed now to determine the expected CG bias in *Euclid* shape measurements using realistic galaxy populations. To do so, we employ HST/ACS data taken in the F606W and F814W filters in the three CANDELS fields (AEGIS, COSMOS, and UDS), which have a roughly homogeneous coverage in
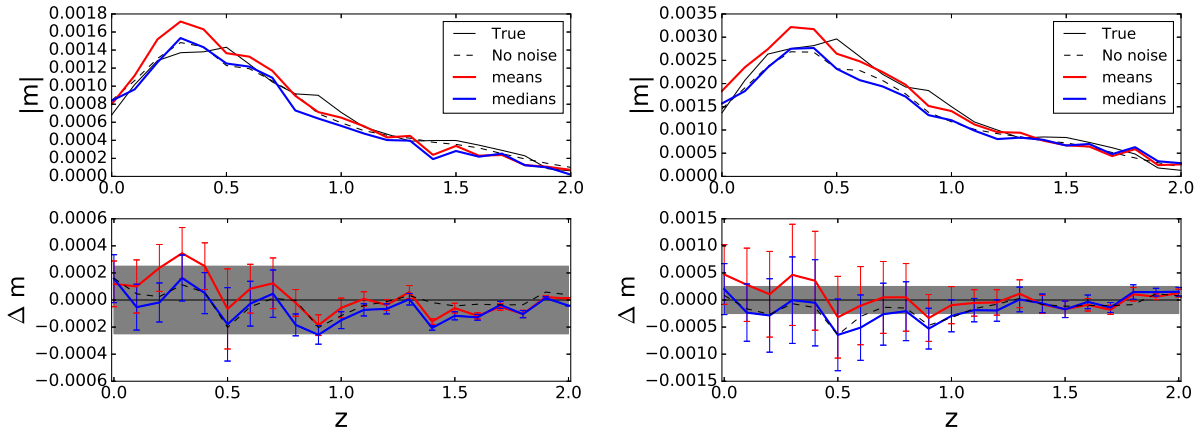
Figure 7. Same as Fig.5 but for images of SNR=15. The red curve shows the mean bias, whereas the blue curve corresponds to the median. To compute the error bars, 1000 realizations are used at each redshift bin for both B- and S-galaxy.
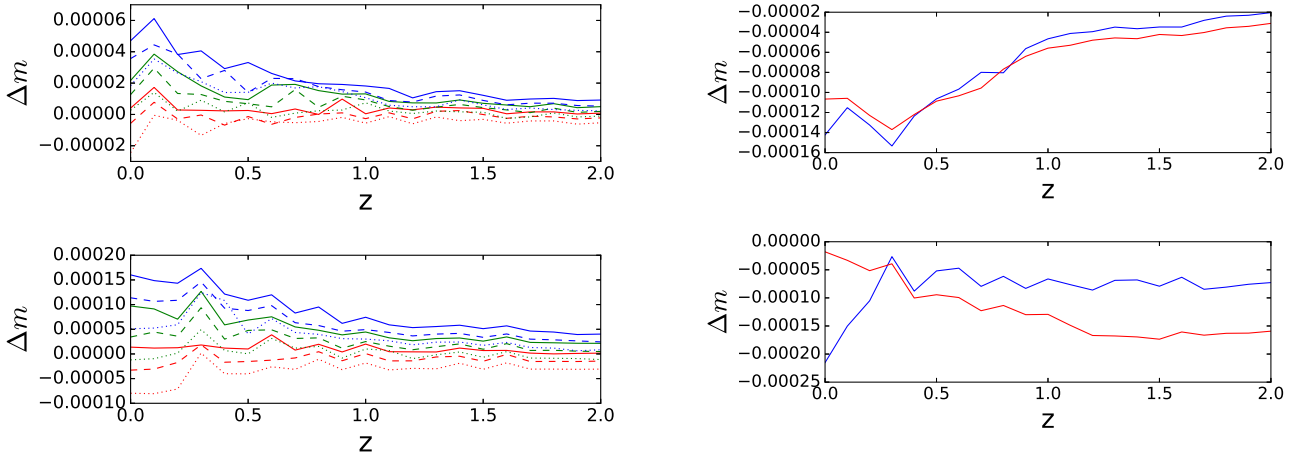
Figure 8. Change in multiplicative CG bias when the size of the PSF used in the deconvolution of the narrow band images is increased (the FWHM differs by 0.9% between steps). From red, green to blue lines, we increase the size of PSF for the F814W filter; from the solid, dashed to dotted lines we increase the size of PSF for the F606W images.

Figure 9. Comparison of PSF between TinyTim model and stars. Top (Bottom) is for the B-galaxy (S-galaxy). The solid (dashed) lines are the result using undrizzled (drizzled) PSF. The dotted lines are that if we also include binary PSF effect.

both bands (see Davis et al. 2007; Grogin et al. 2011; Koekemoer et al. 2011).

We base our analysis on a tile-wise reduction of the ACS data, incorporating pointings that have at least four exposures to facilitate good cosmic ray removal, yielding combined exposure times of 1.3-2.3ks in F606W and 2.1-3.0ks in F814W. We employ the updated correction for charge-transfer inefficiency from Massey et al. (2014), `MultiDrizzle` (Koekemoer et al. 2003) for the cosmic ray removal and stacking, as well as careful shift refinement, optimised weighting, and masking for stars and image artefacts as detailed in Schrabback et al. (2010). Schrabback et al. (2016) created weak lensing catalogues based on these images, and we refer to this paper for more detail. We base our analysis on the galaxies that pass their source selection and apply additional magnitude cuts as detailed below. To investigate the dependence of the colour gradient influence on galaxy colour and redshift, we match this galaxy catalogue to the photometric redshift catalogue from Skelton et al. (2014).

To resemble the selection of galaxies in the *Euclid* wide survey, we derive an approximate estimate for the flux in the VIS-band using:

$$f_{\mathrm{VIS}} = f_{606} + 0.55\left(f_{606} - f_{814}\right), \qquad (16)$$

where f_{606} and f_{814} are the total fluxes from Skelton et al. (2014) and convert this to a magnitude. This estimate is a simple linear interpolation of the fluxes in the two HST filters to the adopted central wavelength of VIS, which we took to be 735 nm (which defines the slope of 0.55). We select galaxies brighter than $m_{\mathrm{VIS}} = 25$. The resulting sample sizes for the three CANDELS fields are listed in Table 2. The number densities are in line with expectations for *Euclid* (Laureijs et al. 2011). Most galaxies in our sample are detected with an $SNR > 15$, and we thus expect to be able to determine the CG bias accurately. In Fig. 10 we present histograms of some of the relevant galaxy properties for the three fields. We observe no significant differences, but note that we find more blue galaxies in AEGIS.
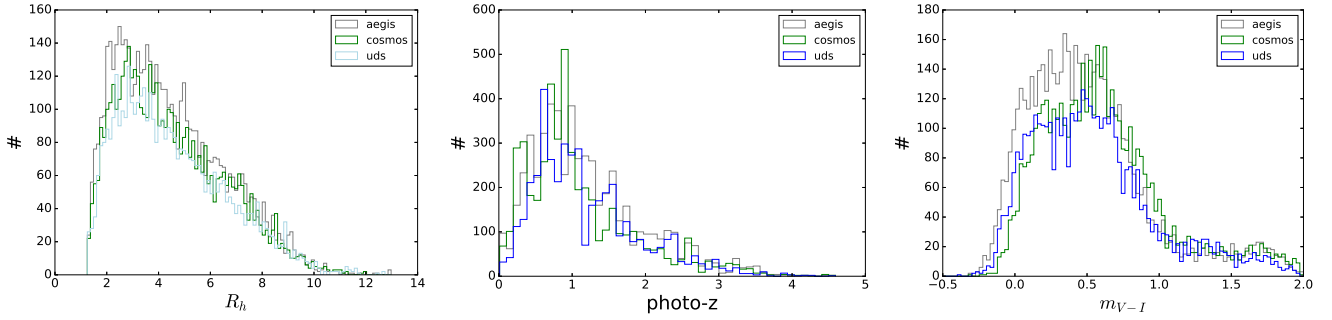
Figure 10. Histogram of the distributionsin observed half-light radii (R_{h}; left panel), photometric redshift (middle panel) and F606W-F814W colour (right panel) for the three CANDELS fields (AEGIS, COSMOS, UDS). We show results for galaxies with $m_{\mathrm{VIS}} < 25$.

Field	AEGIS	COSMOS	UDS	Total
Area [arcmin^2]	180	139	146	465
Total number	5518	4794	4311	14623
Number density [arcmin^{-2}]	30.7	34.5	29.5	31.4

Table 2. Properties of the sample of galaxies selected in the HST CANDELS fields. We select galaxies with $m_{\mathrm{VIS}} < 25$.

4.1 CG bias from CANDELS

We now proceed to apply the procedure we tested on synthetic galaxies on the HST observations to determine the expected CG bias for *Euclid*. We use the default TinyTim when we fit the single component Sérsic models to the observations using GALFIT. We adopt priors on the Sérsic index ($0.5 < n < 5.0$), the effective radius ($1 < r_e < 50$ pixel) and axis ratio ($0.6 < q < 1.0$). We assume that the Airy model (Eq. 9) is a good representation of the *Euclid* PSF. As described in 3.2 we interpolate the SED on each pixel of the model galaxy to generate a wavelength dependent image (Eq.10 - 12), which is integrated and convolved to create the images with and without colour gradients. We create images with six different orientations to reduce estimate the multiplicative shear bias m caused by colour gradients.

The top panel of Fig. 11 shows the histogram of the CG bias for the three CANDELS fields that we study here. The mean bias is **give the mean bias** and the distribution is quite peaked, with bias less than 0.01 for 94% of the galaxies. Note that the observed distribution will be slightly broadened due to noise in the HST images (cf. the red histogram in Fig. 6). For reference we show in the bottom panel of Fig. 11 the histogram if we adopt a weight function that is twice as large ($2 \times r_{\mathrm{h}}$) to measure the shapes. As expected, the bias decreases by about one order of magnitude. Although an increase in the width of the weight function is thus a potentially interesting approach to reduce the impact of the CG bias, we note that our nominal implementation already suggests that the average bias is small.

The amplitude of the CG bias depends on a number of parameters, such as the redshift and colour. Hence it is not sufficient to consider the average bias for the source sample. We therefore need to explore such trends using our HST measurements. We start with two quantities that should be directly related to the CG bias, namely the ratio of the Sérsic index in the two HST filters and the ratio of the effective radii in the two band.

The colour gradients as a tracer of galaxy evolution have been
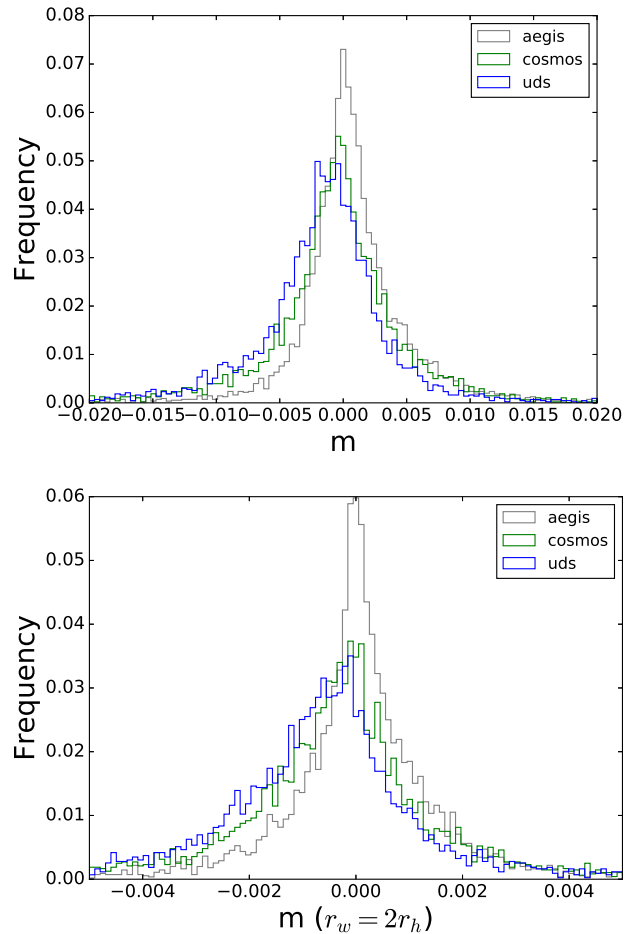
Figure 11. Histogram of the estimated multiplicative bias caused by colour gradients using HST observations. The results for the three different CANDELS fields are indicated by the different colours. The top panel shows the distribution for our nominal choice for the width of the weight function, whereas the bottom panel shows that increasing the width to twice the half-light radius reduces the biases by an order of magnitude.

found to be correlate with some aspects. We try to explore relations between CG bias and the properties of galaxy. First we show the relation between CG bias with two tracers of the colour gradients: the ratio of Sersic index from two bands, and the ratio of
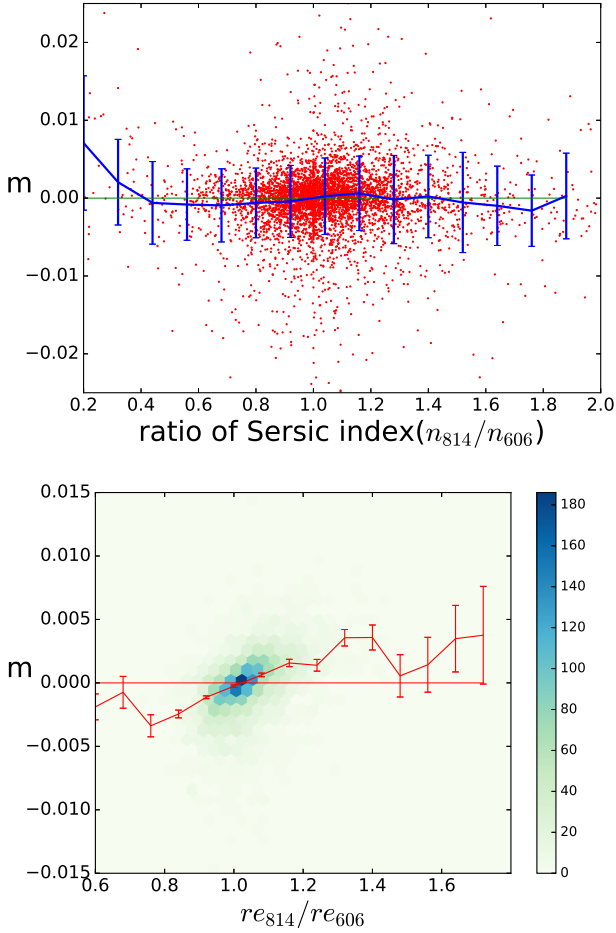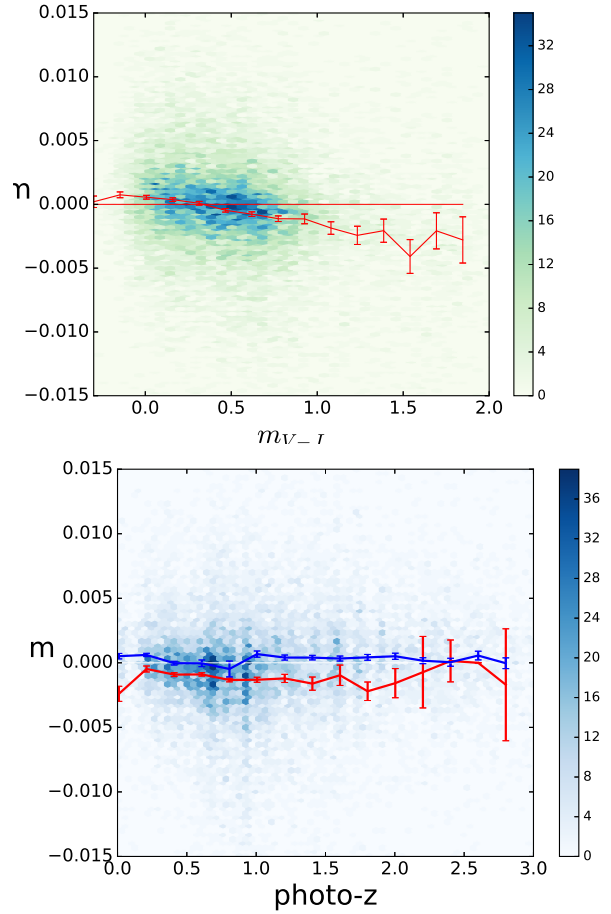
Figure 12. CG bias as a function of galaxy properties: ratio of Sersic index between two band (top) and effective radius between two bands (bottom). The blue lines are the average CG bias over the parameter bins.

Figure 13. CG bias as a function of galaxy properties, top: color (m_{V-I}), bottom: photo-z. In the bottom panel, the red and blue points are the bias for red ($m_{V-I} > 0.5$) and blue ($m_{V-I} < 0.5$) galaxies respectively. The lines are the average CG bias in the redshift bins.

effective radius from two bands (Fig. 12). One can see that there is a linear relation between the bias and the radius, but for that of Sersic index it is not obvious. The reason is that the Sersic index is mainly account for the type of the galaxy, the radius correlates with the colour gradient directly. Moreover, the CG bias depends on several factors of the galaxy, e.g. the total size of the galaxy. It is not surprise to see large bias scatters for the whole sample. In principle, one expect that when $r_{e606} = r_{e814}$ and $n_{606} = n_{814}$, the CG bias in principle will be vanish, since the identical images from two bands will not have a colour gradient. This is confirmed in our result: the blue line (bin average) in Fig. 12 meets zero at $r_{e814}/r_{e606} = 1$. However, those colour gradients information will not be available in Euclid. We also need the relation between the bias with other parameters.

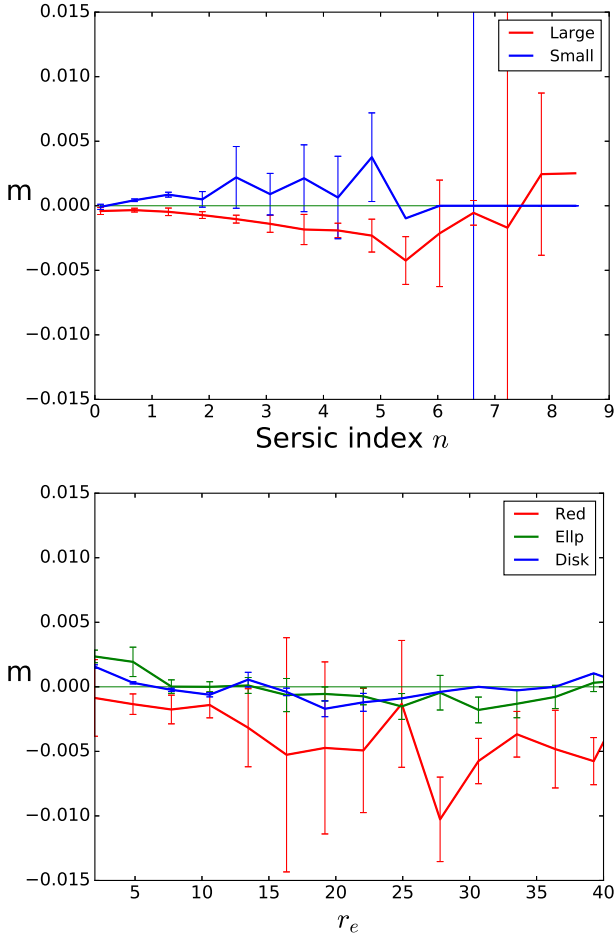The study of the synthetic galaxies already indicated that the CG bias depends

In Fig.11, the galaxies in AEGIS field have more positive CG bias than the galaxies in the other two. The colour distribution in AEGIS is different from the other two as well, which suggests the correlation between the CG bias and the colour of the galaxy. In Fig.13, we show the relation between the CG bias and the colour of the galaxies. The bias is inversely proportional to the colour of the galaxies. This is consistent with the trend of total colour (e.g.

Tortora et al. 2010): the bluer galaxies have positive colour gradients, while the redder ones have negative gradients. Since this marks a possible transition of two types of galaxies, we split the galaxy sample into two groups according to their colour: the red galaxies ($m_{V-I} > 0.5$) and the blue ones ($m_{V-I} < 0.5$). They are shown in the bottom panel of Fig.13 as a function of redshift. Most of the red galaxies are located at moderate redshifts, mainly between redshift [0.5, 1.0], while the blue galaxies are either at the lower redshift ($z < 0.5$) or higher redshift ($z > 1.0$). The CG bias in red galaxies are obviously more negative than that of the blue ones. It again confirms that the colour/colour gradients is an important tracer of the galaxy evolution, since apparently galaxies at different redshift proceed at different stages of the evolution.

The VIS image, on the other hand, contains more information Fig.14 shows the CG bias with the Sersic index and the effective radius fitted from the VIS images. In the top panel, we divide the sample into two groups by the fitted effective radius, either larger or smaller than 0.35 arcsec. The small (large) galaxies are shown by the blue (orange) points, and the blue (red) line is the bin average. The large galaxies cover a large range of Sersic index, have negative average CG bias. Most of small galaxies have small Sersic index (< 2.5). The bias of small galaxies are positive and approx-

photo-z	$Number$	$\bar{m}$	σ_m
$0-0.4$	187	-1.3×10^{-3}	0.012
$0.4-0.8$	1415	-7.6×10^{-4}	0.011
$0.8-1.2$	1116	-1.0×10^{-3}	0.017
>1.2	245	-2.1×10^{-3}	0.015
$0-0.4$	667	6.6×10^{-4}	0.0026
$0.4-0.8$	513	2.8×10^{-4}	0.0028
$0.8-1.2$	187	1.2×10^{-3}	0.0041
>1.2	935	5.4×10^{-4}	0.0046

Table 3. The number, average CG bias and dispersion in redshift bins for blue (bottom half) and red (top half) galaxies.

and CG bias, the experience from photometric redshift can be used for CG bias, such as some machine learning algorithms.

We calculate the average bias and the dispersions over the redshift bins for both red ($m_{V-I} > 0.5$) and blue galaxies (Table 3). The red galaxies are mainly located between redshift $(0.4, 1.2)$, while the blue galaxies are low density in redshift $(0.8, 1.2)$. The bias from red galaxies are significantly smaller than that of blue galaxies, as one expected, the colour gradient in the elliptical galaxies are smaller. The dispersions of the bias in each bin are large, which probably indicate that in each bin there are several kinds and sizes of galaxies. Therefore, in order to calibrate the bias with high precision, one need bigger galaxy samples. From our simulation, we need about 200 galaxies for one type of galaxy in every redshift bin. If we make rough bins, for instance, 2 types of colour: red and blue; 5 different sizes from about 0.1 arcsec to 1.0 arcsec (Fig.14), and 5 redshift bins, at least 20000 galaxies are required. For more realistic SED classifications and redshift bins, several times larger sample are also necessary.

5   SUMMARY AND DISCUSSION

In the image survey for weak gravitational lensing, the wide band filter can provide high signal-to-noise images and large coverage of redshift range. There is however a shape bias due to the chromatic shape of galaxy and the PSF, which is named as colour gradient bias. For very wide band surveys, such as Euclid, this effect can cause a non-negligible bias. In this work, we exam such a kind of bias in measuring the shape of a galaxy using both simulated images and real data taken from the HST ACS CANDELS survey. In the simulated galaxy images, we confirm the bias behaviour from previous results (S13). We further apply the calibration method to the noisy images in the simulations, and find that with reasonable signal-to-noise ratio (SNR= 15) and sufficient numbers of galaxies (300 images for one type of galaxy in one redshift bin), we can estimate the CG bias to a high precision. However, the underestimate cannot be avoided due to strong emission lines, or the uneven SED of source galaxies. Moreover, the simulations are performed with only two galaxy models, and the SNR of the simulated images in two bands are assigned with equal value. In reality, the relation between the SNR with the size and SED of the galaxies has to be taken into account. We also perform comparison of TinyTim and star PSF models. The inaccuracy, especially that due to the binary stars, will cause errors in estimating the CG bias.

In the estimation using CANDELS data, we select the images from two filters (F606W, F814W). For most of the galaxy, the bias ($|m|$) is smaller than 0.01. As we find from simulated images, the

Figure 14. CG bias with Sersic index (top) and effective radius (bottom) from the mock VIS images. The unit of radius is a pixel (= 0.05 arcsec). In the top panel, the blue (red) is the average of small (big) galaxies. In the bottom panel, the red line is average bias of red galaxy ($m_{V-I} > 1$); the green line is that of elliptical galaxy ($n_{Sersic} > 2.75$); the blue line is for the disk galaxy.

imately proportional to the Sersic index. The scatters of the bias for large and small galaxies increase with the Sersic index. In the bottom panel, the galaxies are divide into three groups: the first is red galaxy whose color is large ($m_{V-I} > 1.0$); the second and third group are the rest galaxies either with large Sersic index ($n > 2.25$, elliptical galaxy) or small Sersic index (disk galaxy). The solid lines show the bin average over effective radius. We can see that the VIS image alone can also provide an rough estimation for CG bias, but classification of the galaxies is necessary. As shown in the figure, the disk galaxies have small bias, small radius (< 1 arcsec), and also small bias scatters. The elliptical galaxies cover large radius range, and the bias is larger than the disk ones. The bias in red galaxies are significant, and mainly negative. The scatters of red galaxies are larger than the other two kinds of galaxies. Extra photometry can definitely provide more constraints on the CG bias, as it has been shown the correlations between colour gradients and other properties of galaxy. Moreover, the multi-band information is required for the photometric redshift study. One can obtain that for free to calibrate the CG bias. Although the dependence on the multi-band is different between photometric redshift

estimation using noisy image has a large scatter, thus the CG bias in reality may be even smaller than that shown here. In our sample of galaxies, the CG bias shows a correlation with the colour of galaxies, and a linear relation with the ratio of two band images. We also generate the mock VIS band images. From the parameters of the image (Sersic index and effective radius), one can classify the galaxy in order to obtain tighter constraints on the bias. For example, the galaxies with small Sersic index, i.e. disk-like, have smaller CG bias. On the other hand, those with large Sersic index have large bias and also bias variation. The relations show consistent results about the colour gradient dependence on the properties of galaxy (e.g. Tortora et al. 2010). However, since the CG bias also depends on the relative size with respect to the PSF, the dependence of CG bias is certainly more complicate. We did not provide any fitting formula for the bias at current sample, since the scatters are too large. More importantly, it has to be performed according to the types or morphology of the galaxies, which require larger sample of data.

The multi-band photometry from several bands, which can be used to estimate the redshift, can be also use for the CG bias analysis. Although the redshift dependence is not significant in our sample of galaxies, this may not be the case for a larger survey, or if we look at the bias according to the type of galaxy. Moreover, the colour of galaxy also indicates the evolution history, or the large scale tide force. It can be also used for the study of intrinsic alignment analysis in weak lensing (e.g. Joachimi et al. 2015). Therefore, the dependence of the CG bias on the colour of the galaxies will further increase the sysmatics of the intrinsic alignment. The detail behaviour will require large cosmological simulations, which is beyond the scope of this paper, but definitely needs further studies for the project such as Euclid.

The role of environment on the colour gradients is not clear. On the one hand, it has been shown that colour gradients depend on the environment where galaxies reside, with steeper colour gradients in poor rather than rich clusters (e.g. La Barbera et al. 2005), which is possible due to the different processes during galaxy formation. On the other hand, in recent study using integral field spectra from SDSS-IV, the metallicity gradients show weak or no correlation with density environment (Zheng et al. 2017). In any cases, close galaxy pairs or nearby bright star(s) may also cause weak brightness/colour gradient, which will affect our estimate for CG bias as well.

In this work, we use the brightness moments to estimate the ellipticity of the galaxy. The PSF correction is not taken into account. The bias thus will appear in every method of measurement. However, the bias using the measurement method for real data will be different, since every method has its own property and weight function. The CG bias will have method-dependent properties as well, although they will in principle have same dependence on the colour gradient of the galaxy images. As the first step of the CG bias analysis, we did not adopt any specific method in order to obtain general properties of the CG bias. Before the real analysis of Euclid data, one needs to study the bias with specific methods and simulated images with real properties in the Euclid weak lensing survey.

ACKNOWLEDGMENTS

REFERENCES

Bacon, D. J., Goldberg, D. M., Rowe, B. T. P., & Taylor, A. N. 2006, MNRAS, 365, 414
Bartelmann, M. & Schneider, P. 2001, Phys. Rep., 340, 291
Bertin, E. & Arnouts, S. 1996, A&AS, 117, 393
Bridle, S. L., Kneib, J.-P., Bardeau, S., & Gull, S. F. 2002, in The Shapes of Galaxies and their Dark Halos, ed. P. Natarajan, 38–46
Coleman, G. D., Wu, C.-C., & Weedman, D. W. 1980, ApJS, 43, 393
Cropper, M., Hoekstra, H., Kitching, T., et al. 2013, MNRAS, 431, 3103
Cypriano, E. S., Amara, A., Voigt, L. M., et al. 2010, MNRAS, 405, 494
Davis, M., Guhathakurta, P., Konidaris, N. P., et al. 2007, ApJ, 660, L1
den Brok, M., Peletier, R. F., Valentijn, E. A., et al. 2011, MNRAS, 414, 3052
Eriksen, M. & Hoekstra, H. 2017, MNRAS, 405, 494
Fenech Conti, I., Herbonnet, R., Hoekstra, H., et al. 2016, ArXiv 1606.05337
Frigo, M. & Johnson, S. G. 2005, Proceedings of the IEEE, 93, 216, special issue on "Program Generation, Optimization, and Platform Adaptation"
Goldberg, D. M. & Natarajan, P. 2002, ApJ, 564, 65
Gonzalez-Perez, V., Castander, F. J., & Kauffmann, G. 2011, MNRAS, 411, 1151
Grogin, N. A., Kocevski, D. D., Faber, S. M., et al. 2011, ApJS, 197, 35
Heymans, C., Grocutt, E., Heavens, A., et al. 2013, MNRAS, 432, 2433
Hildebrandt, H., Viola, M., Heymans, C., et al. 2017, MNRAS, 465, 1454
Hoekstra, H., Viola, M., & Herbonnet, R. 2017, MNRAS, 468, 3295
Huff, E. & Mandelbaum, R. 2017, ArXiv e-prints
Jarvis, M., Sheldon, E., Zuntz, J., et al. 2016, MNRAS, 460, 2245
Jee, M. J., Tyson, J. A., Hilbert, S., et al. 2016, ApJ, 824, 77
Joachimi, B., Cacciato, M., Kitching, T. D., et al. 2015, Space Sci. Rev., 193, 1
Kaiser, N., Squires, G., & Broadhurst, T. 1995, ApJ, 449, 460
Kennedy, R., Bamford, S. P., Häußler, B., et al. 2016, A&A, 593, A84
Koekemoer, A. M., Faber, S. M., Ferguson, H. C., et al. 2011, ApJS, 197, 36
Koekemoer, A. M., Fruchter, A. S., Hook, R. N., & Hack, W. 2003, in HST Calibration Workshop : Hubble after the Installation of the ACS and the NICMOS Cooling System, ed. S. Arribas, A. Koekemoer, & B. Whitmore, 337
Köhlinger, F., Hoekstra, H., & Eriksen, M. 2015, MNRAS, 453, 3107
Krist, J. E., Hook, R. N., & Stoehr, F. 2011, in Proc. SPIE, Vol. 8127, Optical Modeling and Performance Predictions V, 81270J
La Barbera, F., De Carvalho, R. R., De La Rosa, I. G., et al. 2010, AJ, 140, 1528
La Barbera, F., de Carvalho, R. R., Gal, R. R., et al. 2005, ApJ, 626, L19
Laureijs, R., Amiaux, J., Arduini, S., et al. 2011, ArXiv e-prints
Massey, R., Hoekstra, H., Kitching, T., et al. 2013, MNRAS, 429, 661
Massey, R., Schrabback, T., Cordes, O., et al. 2014, MNRAS, 439, 887
Melchior, P., Viola, M., Schäfer, B. M., & Bartelmann, M. 2011, MNRAS, 412, 1552
Miller, L., Heymans, C., Kitching, T. D., et al. 2013, MNRAS, 429, 2858
Nakajima, R. & Bernstein, G. 2007, AJ, 133, 1763
Paulin-Henriksson, S., Amara, A., Voigt, L., Refregier, A., & Bridle, S. L. 2008, A&A, 484, 67
Pence, W. 1999, in Astronomical Society of the Pacific Conference Series,

Vol. 172, Astronomical Data Analysis Software and Systems VIII, ed. D. M. Mehringer, R. L. Plante, & D. A. Roberts, 487

Peng, C. Y., Ho, L. C., Impey, C. D., & Rix, H.-W. 2010, AJ, 139, 2097

Rowe, B. T. P., Jarvis, M., Mandelbaum, R., et al. 2015, Astronomy and Computing, 10, 121

Schrabback, T., Applegate, D., Dietrich, J. P., et al. 2016, ArXiv e-prints

Schrabback, T., Hartlap, J., Joachimi, B., et al. 2010, A&A, 516, A63

Semboloni, E., Hoekstra, H., Huang, Z., et al. 2013, MNRAS, 432, 2385

Skelton, R. E., Whitaker, K. E., Momcheva, I. G., et al. 2014, ApJS, 214, 24

Tortora, C., Napolitano, N. R., Cardone, V. F., et al. 2010, MNRAS, 407, 144

Voigt, L. M., Bridle, S. L., Amara, A., et al. 2012, MNRAS, 421, 1385

Zheng, Z., Wang, H., Ge, J., et al. 2017, MNRAS, 465, 4572